Materials Advances

ROYAL SOCIETY OF CHEMISTRY

PAPER

View Article Online
View Journal | View Issue

Cite this: *Mater. Adv.*, 2024, 5, 2359

Molecular stacking mode-directed mechanical compliance and room-temperature phosphorescence achieved by polymorphic 4-cyanobenzamide crystals†

Di Wang,[a] Hui-Min Tang,[a] Bo Ding,[a] Xiu-Guang Wang,[a] Haijiao Xie[b] and En-Cui Yang *[a]

Organic molecular crystals with both excellent room-temperature phosphorescence (RTP) and adaptive mechanical compliance are of particular importance in flexible photonic materials and devices but remain challenging because of the complexity and sensitivity of molecular stacking modes driven by weak intermolecular interactions. To understand the underlying mechanism for the dual-functional integration on a molecular level, two polymorphs of 4-cyanobenzamide (CN-BZM) with the same space group but quite different mechanical responses and RTP emissions have been identified through well-organizing intermolecular hydrogen-bonding interactions. Naturally, straight acicular **Form I**, constructed from an interlocked alignment of π-stacked $\{CN\text{-}BZM\}_2$ columns, exhibits reversibly elastic deformations and unusual time-dependent multicolor afterglow from orange to green over 3 s. However, flaky **Form II** with a parallel displaced arrangement of the π-stacked {CN-BZM} arrays is brittle, emitting only orange RTP with a long-lived lifetime of up to 148.3 ms. Further structural comparisons and theoretical calculations demonstrated that strong hydrogen-bond coupled $\{CN\text{-}BZM\}_2$ dimer, co-planar inclined H-aggregation and interlocked π-stacked arrays in the crystal matrix are collaboratively responsible for the elastic flexibility and multicolor afterglow of **Form I**. Thus, well-organizing intermolecular secondary forces by polymorphic engineering has become one of the powerful methods for elaborating the mechanism of dual-functional organic crystals with adaptive mechanical compliance and persistent luminescence.

Received 12th December 2023,
Accepted 14th January 2024

DOI: 10.1039/d3ma01109g

rsc.li/materials-advances

Introduction

Organic molecular crystals with both persistent afterglow and adaptive mechanical compliance (elasticity or plasticity) have recently attracted considerable interest due to their good tailorability, easy preparation, as well as innovative applications as flexible photonic devices in anti-counterfeiting, displays, and optical waveguides.[1–6] Structurally, the integration of highly efficient room-temperature phosphorescence (RTP) and flexible mechanic response depends essentially on the molecular stacking modes confined by weak intermolecular non-covalent forces.[2,7–13] On the one hand, conformation rigidification in the crystal matrix by hydrogen-bonding, halogen-bonding, C–H···π and π···π interactions has efficiently minimized non-radiative decay and overall quenching rates of triplet excitons, greatly prolonging the long-lived lifetime up to millisecond- and even second-levels.[2] More importantly, strong intermolecular interactions and preferred H-aggregations are capable of effectively optimizing the electronic configurations of the excited states with differing energy levels for frontier molecular orbitals, facilitating the intersystem electronic communications and stabilizing consequently the triplet excited states.[14,15]

Molecular stacking mode, on the other hand, is of great essence for smart mechanical responses of organic crystals.[1,5–7] Due to the limited available crystal data, the intrinsic mechanism of mechanical compliance has not been well understood.[8–10] While it is clear that minor structural changes can lead to drastic changes in mechanic behaviors. Fundamentally, the elastic deformation requires interlocked molecular packing, isotropic intermolecular interaction, and/or fibril

[a] College of Chemistry, Tianjin Key Laboratory of Structure and Performance for Functional Molecules, Tianjin Normal University, Tianjin 300387, People's Republic of China. E-mail: encui_yang@163.com
[b] Hangzhou Yanqu Information Technology Co., Ltd, Y2, 2nd Floor, Building 2, Xixi Legu Creative Pioneering Park, No. 712 Wen'er West Road, Xihu District, Hangzhou City, Zhejiang Province, 310003, People's Republic of China

† Electronic supplementary information (ESI) available. CCDC 2288452 and 2288453. For ESI and crystallographic data in CIF or other electronic format see DOI: https://doi.org/10.1039/d3ma01109g

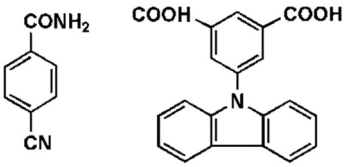

CN-BZM CzIp

Scheme 1 Chemical structures of CN-BZM and CzIp.

lamella morphology to prevent long-range sliding of molecular planes. Thus, skillful manipulations on the stacking mode and strength of the intermolecular interacting force are highly significant and urgently needed. Acting as one of the simplest and widely used methods, crystallization engineering, as compared to polymerization,[16] host–guest complexation,[17] matrix rigidification,[18] crosslinking,[19] and clusterization,[20] is highly effective for re-organizing soft intermolecular interactions as well as lifetime elongation and efficiency enhancement of the RTP performance.[21] To our knowledge, to date, only a few crystalline elastic deformation-RTP systems have been developed, which cover only halogen-, alkoxy-, and/or alkyl-substituted benzyl,[22–24] carbazole/dibenzothiophene[25–28] and benzophenone/xanthone derivatives.[29] In addition to the preferred π-stacked phosphors, all these successful examples benefit structurally from the halogen-involved weak interactions or well-designed divisional aggregation structures. To understand molecular packing-dependent bifunctional composition in-depth, a semi-rigid 4-cyanobenzamide (CN-BZM, Scheme 1) with a rigid phenyl ring, lone-pair electron-abundant, and hydrogen-bonding accessible side-arms, is ingeniously selected to self-assemble by crystallization engineering strategy.[2,21,30,31] As expected, two polymorphic CN-BZM crystals (labeled as **Form I** and **Form II**) with the same space group but distinct morphologies, mechanic responses and RTP emissions have been obtained. The co-relationships between molecular stacking and integrated mechanic compliance-RTP performance are discussed.

Table 1 Crystal data and structure refinement for two polymorphs of 4-cyanobenzamide[a]

Crystal	Form I	Form II
Formula	$C_8H_6N_2O$	$C_8H_6N_2O$
F_w	146.15	146.15
Crystal system	Monoclinic	Monoclinic
Space group	$P2_1/n$	$P2_1/c$
a (Å)	3.7377(3)	7.1484(13)
b (Å)	15.2421(11)	10.7108(13)
c (Å)	12.2673(10)	9.9789(16)
α (°)	90	90
β (°)	96.345(7)	107.365(19)
γ (°)	90	90
V (Å^3)	694.59(9)	729.2(2)
Z	4	4
D_c (g cm^{-3})	1.398	1.331
μ (mm^{-1})	0.791	0.753
F(000)	304.0	304.0
θ range (°)	9.288–134.114	12.436–134.152
$h/k/l$	−3, 4/−18, 18/−13,14	−6, 8/−12, 12/−10, 11
Data/restraints/params	1248/0/100	1301/10/110
R_{int}	0.0231	0.0322
GoF on F^2	1.058	1.045
R_1,[a] wR_2[b] ($I > 2\sigma(I)$)	0.0428, 0.1142	0.0725, 0.2049
R_1, wR_2 (all data)	0.0546, 0.1239	0.0921, 0.2327
Residuals (e Å^{-3})	0.19, −0.23	0.23, −0.37

[a] $R_1 = \Sigma(||F_o| - |F_c||)/\Sigma|F_o|$. [b] $wR_2 = [\Sigma w(|F_o|^2 - |F_c|^2)^2/\Sigma w(F_o^2)^2]^{1/2}$.

Experimental

All raw materials, apparatus for structural characterizations (single-crystal and powder X-ray diffractions (SC-XRD and PXRD), mechanical tests, theoretical calculations, and photoluminescent measurements), and synthetic procedures of the two polymorphic crystals are described in the ESI.† The obtained crystallographic information and refinement parameters are listed in Table 1.

Results and discussion

Syntheses and PXRD patterns

Two polymorphs of CN-BZM with needle-like and lamellar-shaped morphologies were generated by a simple recrystallization method. Note that, acting as a crystal control agent, 5-(9*H*-carbazol-9-yl)isophthalic acid (CzIp, Scheme 1) plays an important role in the re-organizations of weak intermolecular interactions, resulting in a new crystal form. The phase purity of the bulk as-prepared samples was verified by PXRD characterization, in which the experimental curves were well-matched with the simulated ones extracted from the SC-XRD data (Fig. S1, ESI†).

Crystal structure of Form I

Naturally, straight **Form I** crystal with 10–15 mm in length crystallizes from the $P2_1/n$ space group of the monoclinic crystal system (Fig. 1 and Table 1), exhibiting a compact self-aggregate with π-stacked {CN-BZM}$_2$ columns crisscrossed aligned by weak hydrogen-bonding interactions. The asymmetric unit contains only one neutral CN-BZM molecule with a slight twist angle of 20.1° between the amide group and phenyl ring. Two crystallographically identical CN-BZM molecules are closely connected through a pair of strong –NH···O═C hydrogen-bond between the two adjacent amide groups (Table S1, ESI†), resulting in a head-to-head coupled centrosymmetric {CN-BZM}$_2$ dimer with the donor–acceptor distance (d_{N-O}) and the ∠NHO angle of 2.9111(2) Å and 172° (Table S1, ESI†). These hydrogen-bonding parameters are comparable to classic strong hydrogen-bonding interactions between acid and amide/amino synthons.[9,10,30] From the viewpoints of the electronic structure, the middle part of the dimer is a lone-pair electron abundant-amide pair and both ends are electron-rich phenyl rings. The fragment can act as a proton acceptor in intermolecular interactions to favor the intermolecular electron communications between the donor and acceptor moieties.

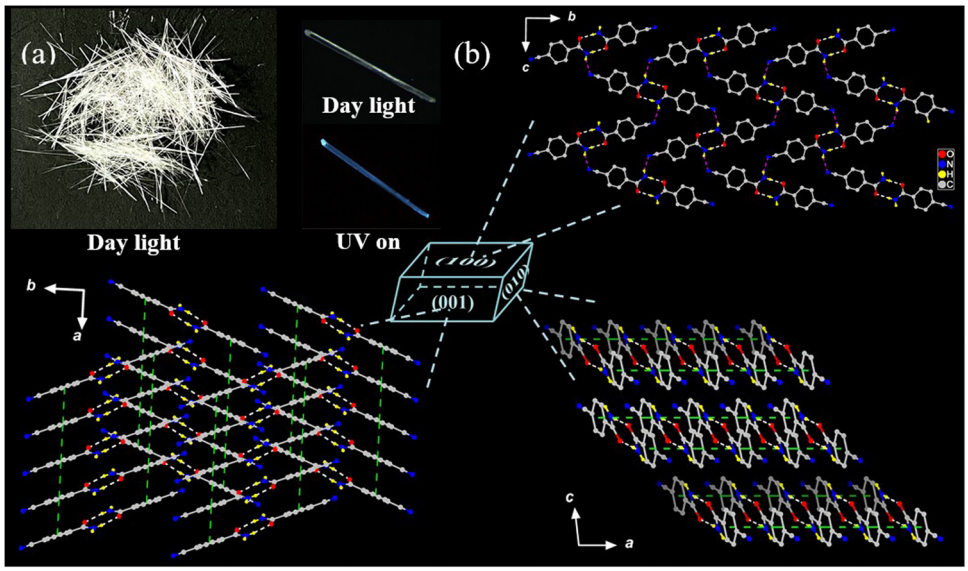

Fig. 1 (a) Digital photos of **Form I** crystals in daylight and UV irradiation. (b) Packing patterns of **Form I** viewed into (100), (010), and (001) faces.

The $\{CN\text{-}BZM\}_2$ dimers are crisscrossed and extended in the crystallographic *bc* plane through weak –NH···N≡C interactions, resulting in a slightly corrugated layer (Fig. 1b). The distance between the donor and acceptor is elongated by 0.08 Å compared to the sum of van der Waals radii (r_w) for two N atoms ($\Delta d_{N\text{–}N} = d_{N\text{–}N} - 2r_{w,N} = 3.18 - 3.10$). While the distance between H and the acceptor is shortened by 0.38 Å than the corresponding sum of van der Waals radii ($\Delta d_{H\cdots N} = d_{H\cdots N} - r_{w,N} - r_{w,H} = 2.37 - 2.75$). Moreover, both the elongated and shortened extent of the intermolecular –NH···N≡C interactions ($\Delta d_{N\text{–}N}$ and $\Delta d_{H\cdots N}$) are more obvious than those of the intra-dimer –NH···O=C interactions ($\Delta d_{N\text{–}O} = d_{N\text{–}O} - r_{w,N} - r_{w,O} = 0.01$ Å, $\Delta d_{H\cdots O} = d_{H\cdots O} - r_{w,H} - r_{w,O} = -0.66$ Å), evidencing the weakened inter-dimer hydrogen-bonding interactions. These dimers are contacted with each other through face-to-face π–π interactions between phenyl rings, thus generating a π-stacked $\{CN\text{-}BZM\}_2$ column along the crystallographic *a*-axis. The centroid-to-centroid distance of the π–π interaction is 3.737(3) Å, and the angle between the transition dipole and connected axis is 75.2° (Table S2 and Fig. S2, ESI†). Apparently, the CN-BZM in **Form I** presents a preferred coplanar inclined H-aggregation.[15] Furthermore, the adjacent columns are orientated in an interlocked crisscrossed manner in the (001) face through soft inter-column –CH···O=C hydrogen-bond with the longest separation of $d_{C\text{–}O}$ = 3.2499(3) Å (Table S1 and Fig. S3, ESI†). Remarkably, these interlocked columns, by –NH···N≡C and –CH···O=C interactions, hopefully induce elastic flexibility when subjected to applied force.[8,10] Moreover, each CN-BZM molecule in the crystalline state is tightly restricted in a rigid environment by

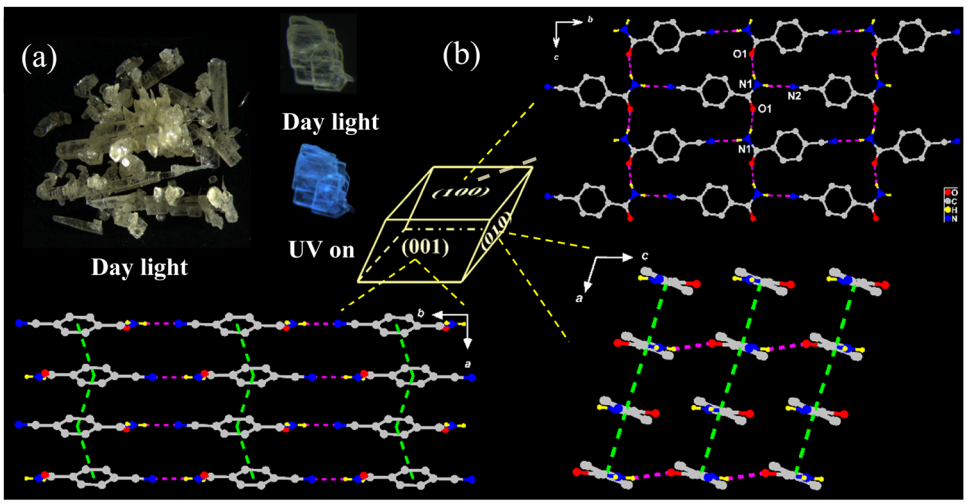

Fig. 2 (a) Digital photos of **Form II** crystals in daylight and UV irradiation. (b) Molecule packings of **Form II** viewed into (100), (010), and (001) faces.

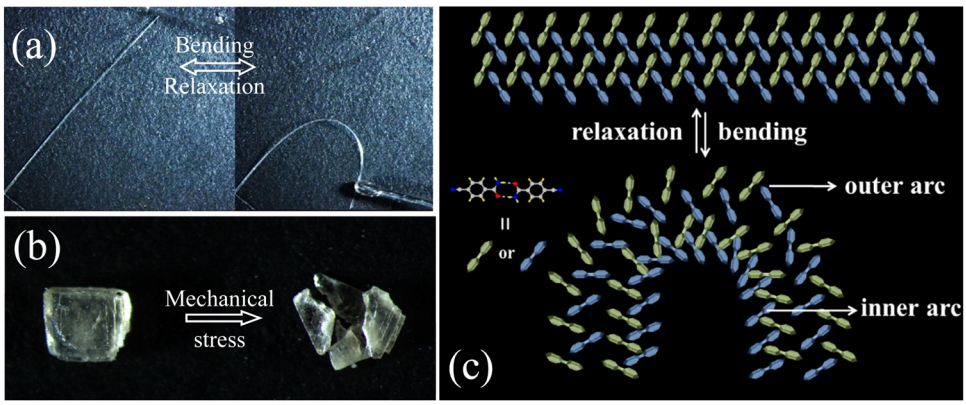

Fig. 3 (a) Screenshots of reversible elastic bending test of **Form I** crystal under mechanical stress applied through a pair of tweezers under daylight. (b) Schematic representation of the molecular rearrangement in **Form I** during the bending state. (c) Fractures of **Form II** crystal upon application of mechanical stress.

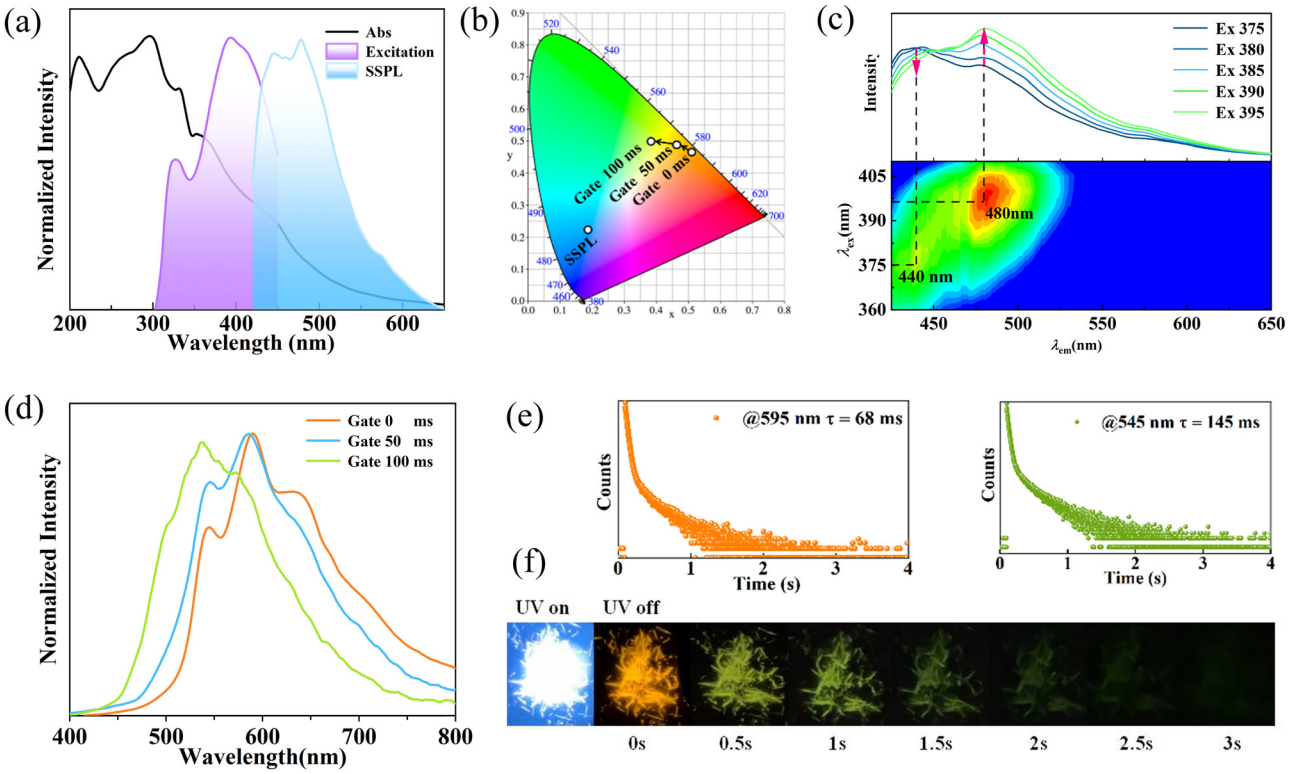

Fig. 4 (a) UV-vis absorption spectrum, the steady-state photoluminescence excitation spectrum at 480 nm, photoluminescence and phosphorescence spectra upon excitation at 385 nm of **Form I** under ambient conditions. (b) CIE coordinate diagrams of **Form I** at the UV light and at the gradually increased gating time. (c) The excitation–emission mapping of **Form I**. (d) Gating time-dependent delayed spectra of **Form I** excited by 365 nm UV light. (e) Transient time-dependent decay curves for **Form I** at 545 and 595 nm. (f) The afterglow of **Form I** under 365 nm excitation.

eight weak intermolecular interactions (Fig. S4, ESI†), and the molecular motion and non-radiative decay pathways of triplet excitons are efficiently suppressed.[2,15,18]

Crystal structure of Form II

Pale-yellow lamellar-shaped **Form II** belongs to the same space group as **Form I** (Fig. 2a and Table 1) but features a loose self-aggregation with π-stacked {CN-BZM}-arrays orientated in an offset parallel displacement fashion. Similar to **Form I**, only one neutral CN-BZM was found in the asymmetric unit with a dihedral angle of 19.384(491)° between the phenyl and amide groups. Differently, the cell parameters vary moderately, with the increased β angle (96.345(7)° *vs.* 107.365(19)°) and the cell volume (694.59(9) *vs.* 729.2(2) Å^3) but the crystal density was decreased (1.398 *vs.* 1.331 g cm^{-3}, Table 1), compared to that of **Form I**. The cell parameters quantitatively confirm a looser

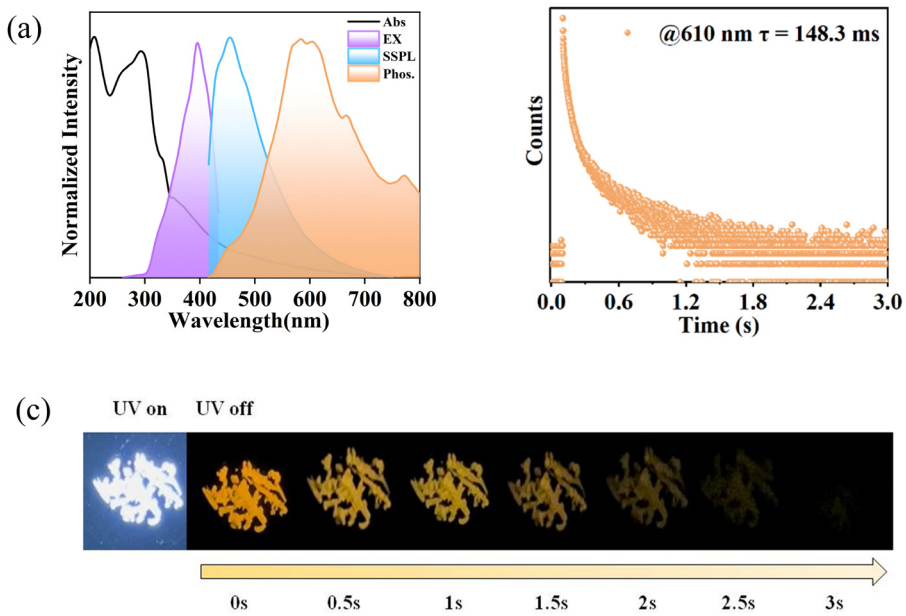

Fig. 5 (a) Solid UV-vis absorption spectra, photoluminescence excitation spectrum at 395 nm, fluorescence emission, and phosphorescence emission spectra of **Form II** at room temperature. (b) Time-resolved emission decay profiles for **Form II** crystal at 454 and 610 nm excited by 395 nm. (c) The afterglow of **Form II** under 365 nm excitation.

molecular aggregation of **Form II** than **Form I**, responsible reasonably for different RTP behavior.[2]

As can be seen in Fig. 2b, each CN-BZM monomer is extended through pairs of orthogonal –NH···O=C and –NH···N≡C hydrogen-bonds, giving rise to a hydrogen-bonded sheet in the (100) plane. The strength of –NH···O=C interaction along the *c*-axis is much stronger than that of –NH···N≡C hydrogen-bond along the *b*-axis (d_{N-O} = 2.868(4) Å *vs.* d_{N-N} = 3.104(4) Å, $\Delta d_{N-O} = -0.03$ Å *vs.* Δd_{N-N} = 0.10 Å, Table S1, ESI†), suggesting intralayer anisotropic interacting forces. Notably, the hydrogen-bonded dimer in **Form I** is absent in **Form II** owing to the re-organizations of intermolecular –NH···N≡C and –NH···O=C hydrogen-bonds.

Along the crystallographic *a*-axis, the adjacent CN-BZM monomers are accumulated together in a head-to-tail manner, leading to a π-stacked array with centroid-to-centroid separation of 3.731(8) Å and the angle of 74.8° between the transition dipole and connected axis (Table S2 and Fig. S5, ESI†). Thus, two adjacent CN-BZM molecules adopt the H-aggregation mode along *a*-axis. Quite different from **Form I**, these π-stacked {CN-BZM} columns are arranged in a parallel fashion, resulting in the supramolecular sheets in (010) and (001) planes (Fig. 2b). Each CN-BZM molecule in **Form II** is tightly frozen by four hydrogen-bonds and the two π–π stackings (Fig. S6, ESI†) are in a slightly less rigid environment than those in **Form I**.

Mechanical responses

The molecular packing of polymorphs is extremely important for the mechanical responses to the applied force.[8,10] The mechanical compliance of the two CN-BZM polymorphs was thus investigated by three-point bending measurements. As shown in Fig. 3a, one end of the **Form I** crystal was first fixed on a plastic plate with tape, and the crystal was in a naturally straight state. Then, the other free end of the crystal was pushed gently with a needle. With the gradual increase of the external force, the straight **Form I** crystal exhibited a distorted arc with a maximum curvature exceeding 90°. When the needle was taken away, the bendable crystal returned quickly back to its pristine straight state. The bending-relaxation process can be repeated several times, thus demonstrating a highly reversible elasticity at room temperature. The entire elastic bending video was recorded under a microscope, which can be seen in the movie S1 of ESI.† However, the **Form II** crystal is fragmented once a small external force is applied on the bulk-exposed surface (Fig. 3b). These mechanical test results suggest that **Form I** is elastic and **Form II** is brittle.

The quite different mechanical responses of the polymorphic CN-BZM crystals are structurally correlated with the π-stacked column and the packing patterns of the adjacent columns in the crystal matrix. During the bending process of **Form I**, the interplanar distance of the π-stacked $\{CN\text{-}BZM\}_2$ array along the crystallographic *a*-axis is elongated and compressed in the outer and inner arcs (Fig. 3c). When the crystal is relaxed to the naturally straight state, the process is opposite. The interlocked nature of the adjacent $\{CN\text{-}BZM\}_2$ columns in **Form I** by weak –NH···N≡C and –CH···O=C hydrogen bonds act as a structural buffer to prevent the long-range sliding of the aromatic planes and ensure the reversible elasticity.[8,10] The parallel alignment of the {CN-BZM} arrays and anisotropic hydrogen-bonded layer parallel to the crystallographic *bc* plane makes **Form II** fragile.

RTP emissions

Photophysical properties of the polymorphic CN-BZM crystals were investigated to explore the aggregation mode-dominated

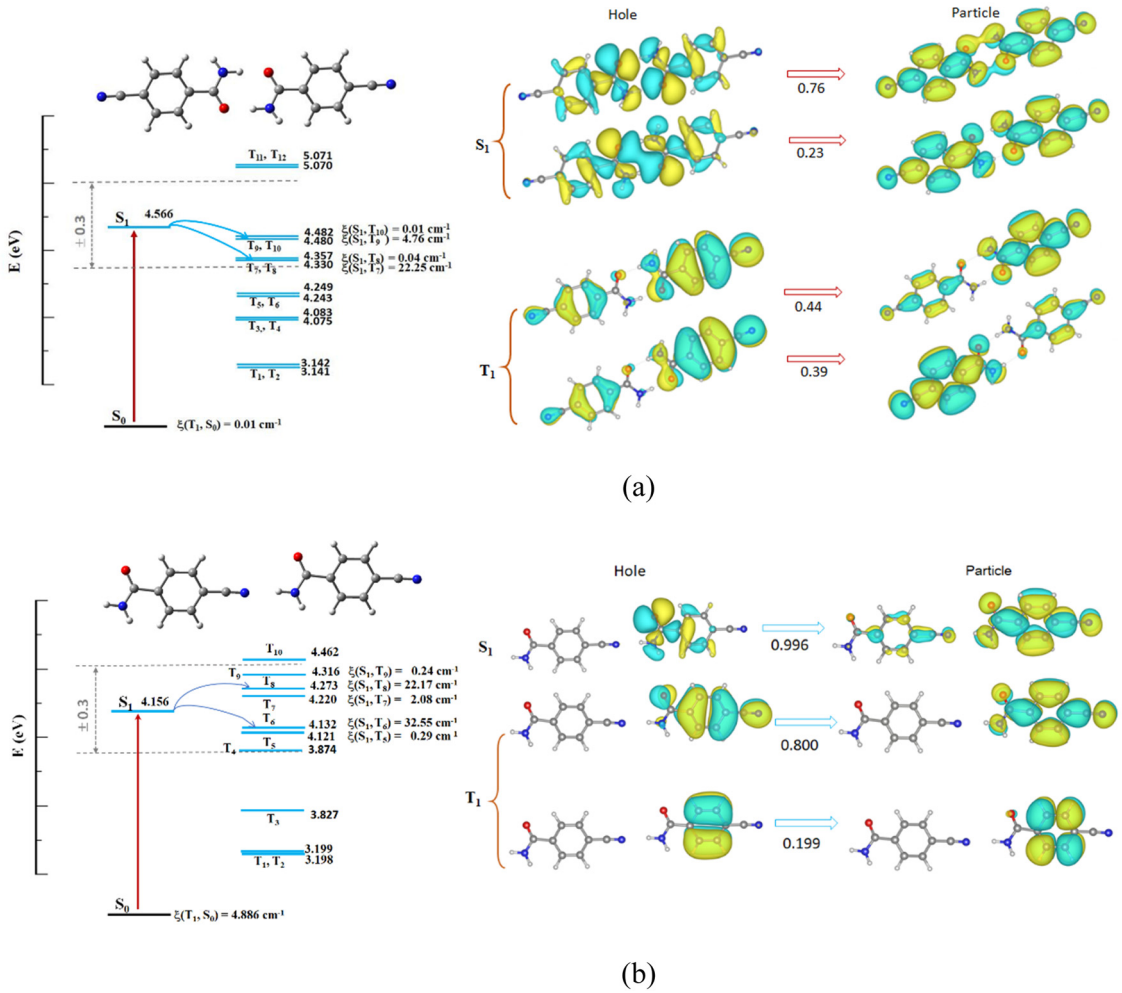

Fig. 6 The calculated energy level diagrams, SOC matrix elements (ξ), and natural transition orbitals (NTO) analyses for the S_1 and T_1 states of two hydrogen-bond coupled dimers in **Form I** and **Form II**.

RTP responses. As illustrated in Fig. 4a, the **Form I** crystal shows a broad UV absorption ranging from 200 to 600 nm with a main band at 300 nm and a shoulder peak at 332 nm. These absorptions are attributed to π–π* and n–π* transitions of CN-BZM.[30,31] Once irradiated using the 385-nm UV light, **Form I** assumes a broad-band fluorescence emission with two maxima at 440 and 480 nm (Fig. 4a). The intense emission corresponds to a CIE coordinate of (0.382 0.503), and a bright blue light is clearly caught by the naked eyes in both the naturally straight and elastic bending states (Fig. 1a and 4b and Fig. S7, ESI†). The short fluorescence lifetime (τ) is 2.19 ns, monitored at 440 nm (Fig. S8, ESI†). On emission at 480 nm, two excitations with distinct intensities were found at 320 and 400 nm, implying the excitation-dependent emission behavior of **Form I**. As the excitation wavelength increases from 375 to 395 nm, the crystal displays an apparent red-shift trend from 440 to 480 nm (Fig. 4c). These observations confirm that the excitation-dependent fluorescence emissions of **Form I** are due reasonably to the multiple absorption energy levels of CN-BZM.

Upon excitation at 365 nm using the UV light, the delay spectrum of **Form I** without gate time displays three emissions with a main peak at 595 nm and two shoulder bands at 544 and 636 nm (Fig. 4d). The emission spectrum corresponds to a CIE coordinate of (0.505 0.469) in the red region (Fig. 4b). Interestingly, with the elongation of the gate time up to 100 ms, two low-energy emissions at 595 and 636 nm are gradually weakened, and the pristine weak peak at 544 nm becomes stronger (Fig. 4d). Correspondingly, the CIE coordinates move towards green region, from (0.468 0.489) slowly to (0.382 0.503). The orange RTP has a lifetime of 68 ms at 595 nm, while the green RTP has a longer lifetime of 145 ms at 545 nm (Fig. 4e). The quantum yield (Φ) of **Form I** calculated using the integrating sphere method is 8.5%, in which the phosphorescence lifetime is 2.8% (Φ_P = 2.8%).

Upon irradiation using a 365-nm hand-portable UV lamp, **Form I** can emit a bright white fluorescence (Fig. 4f). When the UV light was turned off, the afterglow was orange and then rapidly turned to green within 400 ms. The green afterglow completely fades over 3 s. These observations indicate that **Form I** has time-dependent multicolor afterglow, which has been observed only in the crystalline bis-carbazole, cytosine, and melamine-based systems.[32–34]

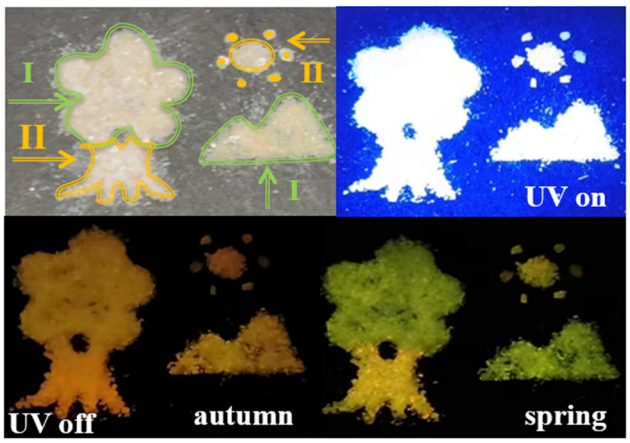

(a)

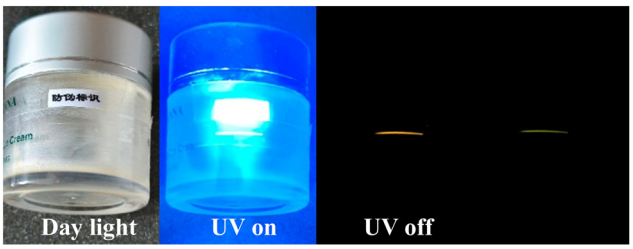

(b)

Fig. 7 (a) Time-dependent colorful display of a landscape painting built from two polymorphs. (b) Demonstration of the elastic **Form I** crystal for anti-counterfeit application on the curved surface.

Form II has similar UV absorptions with **Form I** due to π–π* and n–π* transitions (Fig. 5a). Upon incidenting the UV radiation of 395 nm, **Form II** exhibits a strong sky-blue fluorescence at 454 nm with a short-lived lifetime of only 2.10 ns (Fig. 2a and 5a, Fig. S9 and S10, ESI†). Under the same excitation conditions, **Form II** emits an orange light centered at 610 nm with a lifetime of up to 148.3 ms (Fig. 5a and b), suggesting a phosphorescence emission. The absolute quantum yield of the emissive **Form II** is 14.8%, in which the phosphorescence yield is 2.9%. Furthermore, an ultra-long orange afterglow was observed after turning off the UV light, which completely disappears within 3 s (Fig. 5c). Thus, as compared with **Form I**, **Form II** with a loose self-aggregation emits only a red-shift RTP with a comparable lifetime to **Form I**.

Theoretical calculations

To quantitatively understand aggregation mode-dependent electronic structure and RTP behavior, both the singlet and triplet structures of the isolated monomer and two $\{CN\text{-}BZM\}_2$ dimers were studied using the time-dependent density functional theory (TD-DFT). The initial geometries were extracted from the SC-XRD data and the calculation details are presented in the ESI.†

For the triplet state of the monomer, the three T_n molecular orbitals (n = 3, 4, and 5) have small energy gaps between T_n and S_1 less than 0.3 eV (ΔE_{ST}, Fig. S11, ESI†), indicating three potential intersystem crossing (ISC) channels.[35] Moreover, the three spin–orbit coupling (SOC) matrix elements ξ between T_n and S_1 are larger than 5.55 cm^{-1}, ensuring that more triplet excitons are populated by the three ISC pathways. However, natural transition orbitals (NTO) analyses reveal that the electron transfer for the S_1 state of the monomer occurs from n to π* with 99.7% probability. Similar electron transfer can be observed for the T_1 state of the monomer with 82.8% probability (Fig. S11, ESI†). Apparently, the spin–flip transition occurs from $^1(n \rightarrow \pi^*)$ to $^3(n \rightarrow \pi^*)$, which is spin-forbidden based on the EI-Sayed rule.[2] Therefore, no effective ISC process occurs for the CN-BZM monomer, in agreement with the experimental results of the CN-BZM-doped PVA film with 0.1 wt% concentration.

For the triplet state of the head-to-head coupled dimer, there are four T_n MOs (n = 7, 8, 9, and 10), which have suitable energy gaps for the potential ISC process. Only two ISC pathways ($S_1 \rightarrow T_7$ and $S_1 \rightarrow T_9$) are effective because of the larger ξ values of 22.25 and 4.76 cm^{-1} (Fig. 6a). On the other hand, the NTO analyses indicate that n → π* and π → π* transitions of the spin-flipping occur for the S_1 and excited triplet states (Fig. 6a). Thus, the strong hydrogen-bond connected dimer has a spin-allowed ISC process from $^1(n, \pi^*)$ to $^3(\pi, \pi^*)$ responsible for intense RTP emission.[2]

For the weak –HN···N≡C connected dimer in **Form II**, the level splitting of the triplet state is more obvious than that of strong H-bonded $\{CN\text{-}BZM\}_2$. Six T_n orbitals (T_4–T_9, Fig. 6b) have well-matched energy levels for ISC, and only two transitions $S_1 \rightarrow T_6$ and $S_1 \rightarrow T_8$ with larger ξ coefficients (32.55 and 22.17 cm^{-1}) are effective. The active ISC process is a spin–flip-allowed transition from $^1(n, \pi^*)$ to $^3(\pi, \pi^*)$ by the NTO analyses (Fig. 6b), consistent with the head-to-head connected dimer in **Form I**. These calculated results confirm that the two dimers by directional hydrogen bonds with well-tunable strength play important roles in the ISC transition and resultant RTP property.

Applications

Time-dependent afterglow colors of the two polymorphic crystals can be potentially used in the dynamic color display. As shown in Fig. 7a, a landscape painting is manually produced with the two polymorphic crystals, in which the leaves and the mountain are piled up by **Form I**, and the trunk and sun are amassed with **Form II**. The painting was then illuminated with a 365-nm UV light, and a bright white image was clearly observed with the naked eye. After removing the UV light, the image turns orange, thus demonstrating the scenery of autumn. Interestingly, the leaves and the mountain become immediately green 30 ms later, indicative of a view of spring. Additionally, an anti-counterfeiting application on the curved surface of the cosmetic bottle is developed with the flexible **Form I**. The crystal was carefully attached to the surface of the cylindrical cosmetic bottle. Owing to the elastic flexibility, the **Form I** crystal fits perfectly with the circular surface without fracture (Fig. 7b), showing a colorless transparent crystalline state. When irradiated with a 365-nm UV lamp, the crystal

emits an intense white fluorescence. After the UV lamp is removed, the crystals exhibit a discolored afterglow from orange to green and can be used for anti-counterfeiting. The crystal with reversible elasticity and multicolor afterglow is easy to prepare, showing great application in the field of flexible anti-counterfeiting.

Conclusions

Two polymorphs of CN-BZM with naked-eye distinguishable morphologies were obtained by well-tunable recrystallizations, successfully achieving the molecular packing pattern-dominated hierarchical manipulations on RTP and mechanic compliance. Needle-like **Form I** assembled from the interlocked crisscrossed arrangement of the π-stacked $\{CN\text{-}BZM\}_2$ columns, exhibited time-dependent afterglow from orange quickly to green over 3 s and reversibly elastic flexibility beyond a semi-circle shape. Instead, the lamellar **Form II** with parallel displacement arrangement of π-stacked {CN-BZM} arrays is highly brittle, exhibiting only orange RTP emission with a lifetime of up 148.3 ms. Apparently, the packing modulations of organic molecules are extremely important for the elastically bendable crystals with persistent afterglow.

Conflicts of interest

The authors declare no competing financial interest.

Acknowledgements

Financial supports were received from the National Natural Science Foundation of China (Grant 21571140) and the Program for Innovative Research Team in the University of Tianjin (TD13-5074).

References

1 Y. Wang, L. Sun, C. Wang, F. Yang, X. Ren, X. Zhang, H. Dong and W. Hu, Organic crystalline materials in flexible electronics, *Chem. Soc. Rev.*, 2019, **48**, 1492–1530.
2 W.-J. Zhao, Z.-K. He and B.-Z. Tang, Room-temperature phosphorescence from organic aggregates, *Nat. Rev. Mater.*, 2020, **5**, 869–885.
3 (*a*) C. Zhang, H. Dong, C. Zhang, Y. Fan, J. Yao and Y. S. Zhao, Photonic skins based on flexible organic microlaser arrays, *Sci. Adv.*, 2021, **7**, eabh3530-8; (*b*) F. F. Xu, Y. J. Li, Y. Lv, H. Dong, X. Lin, K. Wang, J. Yao and Y. S. Zhao, Flat-panel laser displays based on liquid crystal microlaser arrays, *CCS Chem.*, 2020, **2**, 369–375.
4 (*a*) X. Chu, Z. Lu, B. Tang, B. Liu, K. Ye and H. Zhang, Engineering mechanical compliance of an organic compound toward flexible crystal lasing media, *J. Phys. Chem. Lett.*, 2020, **11**, 5433–5438; (*b*) B. Tang, B. Liu, H. Liu and H. Zhang, Naturally and elastically bent organic polymorphs for multifunctional optical applications, *Adv. Funct. Mater.*, 2020, **30**, 2004116-6.
5 W. Wu, K. Chen, T. Wang, N. Wang, X. Huang, L. Zhou, Z. Wang and H. Hao, Stimuli-responsive flexible organic crystals, *J. Mater. Chem. C*, 2023, **11**, 2026–2052.
6 K. Naim, M. Singh, S. Sharma, R. V. Nair, P. Venugopalan, S. C. Sahoo and P. P. Neelakandan, Exceptionally plastic/elastic organic crystals of a naphthalidenimine-boron complex show flexible optical waveguide properties, *Chem. – Eur. J.*, 2020, **26**, 11979–11984.
7 (*a*) J. Ravi, T. Feiler, A. Mondal, A. A. L. Michalchuk, C. M. Reddy, B. Bhattacharya, F. Emmerling and R. Chandrasekar, Plastically bendable organic crystals for monolithic and hybrid micro-optical circuits, *Adv. Opt. Mater.*, 2022, **11**, 2201518-10; (*b*) A. Vinod Kumar and R. Chandrasekar, Mechanophotonics: fabrication of a 2 × 2 hybrid directional coupler from flexible organic crystals, *J. Mater. Chem. C*, 2023, **11**, 7995–8001; (*c*) M. Annadhasan, A. R. Agrawal, S. Bhunia, V. V. Pradeep, S. S. Zade, C. M. Reddy and R. Chandrasekar, Mechanophotonics: Flexible single-crystal organic waveguides and circuits, *Angew. Chem., Int. Ed.*, 2020, **59**, 13852–13858; (*d*) M. Annadhasan, S. Basak, N. Chandrasekhar and R. Chandrasekar, Next-generation organic photonics: The emergence of flexible crystal optical waveguides, *Adv. Opt. Mater.*, 2020, **8**, 2000959; (*e*) M. Godumala, A. V. Kumar and R. Chandrasekar, Room-temperature phosphorescent organic materials for optical waveguides, *J. Mater. Chem. C*, 2021, **9**, 14115–14132.
8 A. J. Thompson, A. I. Chamorro Orue, A. J. Nair, J. R. Price, J. McMurtrie and J. K. Clegg, Elastically flexible molecular crystals, *Chem. Soc. Rev.*, 2021, **50**, 11725–11740.
9 G. R. Krishna, R. Devarapalli, G. Lal and C. M. Reddy, Mechanically flexible organic crystals achieved by introducing weak interactions in structure: Supramolecular shape synthons, *J. Am. Chem. Soc.*, 2016, **138**, 13561–13567.
10 S. Saha, M. K. Mishra, C. M. Reddy and G. R. Desiraju, From molecules to interactions to crystal engineering: mechanical properties of organic solids, *Acc. Chem. Res.*, 2018, **51**, 2957–2967.
11 K. J. Kalita, S. Mondal, C. M. Reddy and R. K. Vijayaraghavan, Temperature-regulated dual phosphorescence and mechanical strain-induced luminescence modulation in a plastically bendable and twistable organic crystal, *Chem. Mater.*, 2023, **35**, 709–718.
12 (*a*) Q. Li and Z. Li, Molecular packing: another key point for the performance of organic and polymeric optoelectronic materials, *Acc. Chem. Res.*, 2020, **53**, 962–973; (*b*) M. Fang, J. Yang, X. Xiang, Y. Xie, Y. Dong, Q. Peng, Q. Li and Z. Li, Unexpected room-temperature phosphorescence from a non-aromatic, low molecular weight, pure organic molecule through the intermolecular hydrogen bond, *Mater. Chem. Front.*, 2018, **2**, 2124–2129.
13 X. N. Li, M. Yang, X. L. Chen, J. H. Jia, W. W. Zhao, X. Y. Wu, S. S. Wang, L. Meng and C. Z. Lu, Synergistic intra- and intermolecular noncovalent interactions for ultralong organic phosphorescence, *Small*, 2019, **15**, e1903270-5.
14 Y. Miao, S. Liu, L. Ma, W. Yang, J. Li and J. Lv, Ultralong and color-tunable room-temperature phosphorescence based on

commercial melamine for anticounterfeiting and information recognition, *Anal. Chem.*, 2021, **93**, 4075–4083.

15 Z.-F. An, C. Zheng, Y. Tao, R.-F. Chen, H.-F. Shi, T. Chen, Z.-X. Wang, H.-H. Li, R.-R. Deng, X.-G. Liu and W. Huang, Stabilizing triplet excited states for ultralong organic phosphorescence, *Nat. Mater.*, 2015, **14**, 685–690.

16 G. Q. Zhang, J. B. Chen, S. J. Payne, S. E. Kooi, J. N. Demas and C. L. Fraser, Multi-emissive difluoroboron dibenzoylmethane polylactide exhibiting intense fluorescence and oxygen-sensitive room-temperature phosphorescence, *J. Am. Chem. Soc.*, 2007, **129**, 8942–8943.

17 (*a*) W.-L. Zhou, W.-L. Lin, Y. Chen and Y. Liu, Supramolecular assembly confined purely organic room temperature phosphorescence and its biological imaging, *Chem. Sci.*, 2022, **13**, 7976–7989; (*b*) X.-K. Ma and Y. Liu, Supramolecular purely organic room-temperature phosphorescence, accounts, *Chem. Res.*, 2021, **54**, 3403–3414.

18 D. Lee, O. Bolton, B. C. Kim, J. H. Youk, S. Takayama and J. Kim, Room temperature phosphorescence of metal-free organic materials in amorphous polymer matrices, *J. Am. Chem. Soc.*, 2013, **135**, 6325–6329.

19 S. Tao, S. Lu, Y. Geng, S. Zhu, S. A. T. Redfern, Y. Song, T. Feng, W. Xu and B. Yang, Design of metal-free polymer carbon dots: a new class of room-temperature phosphorescent materials, *Angew. Chem., Int. Ed.*, 2018, **57**, 2393–2398.

20 (*a*) Q. Zhou, B. Cao, C. Zhu, S. Xu, Y. Gong, W. Z. Yuan and Y. Zhang, Clustering-triggered emission of nonconjugated polyacrylonitrile, *Small*, 2016, **12**, 6586–6592; (*b*) T. Yang, Y. Li, Z. Zhao and W. Z. Yuan, Clustering-triggered phosphorescence of nonconventional luminophores, *Sci. China: Chem.*, 2023, **66**, 367–387.

21 K. Zhang, C. C. Sun, Y. Liu, C. Wang, P. Shi, J. Xu, S. Wu and J. Gong, Structural origins of elastic and 2D plastic flexibility of molecular crystals investigated with two polymorphs of conformationally rigid coumarin, *Chem. Mater.*, 2021, **33**, 1053–1060.

22 H. Liu, Z. Bian, Q. Cheng, L. Lan, Y. Wang and H. Zhang, Controllably realizing elastic/plastic bending based on a room-temperature phosphorescent waveguiding organic crystal, *Chem. Sci.*, 2019, **10**, 227–232.

23 J. Song, Y. Zhou, Z. Pan, Y. Hu, Z. He, H. Tian and X. Ma, An elastic organic crystal with multilevel stimuli-responsive room temperature phosphorescence, *Matter*, 2023, **6**, 2005–2018.

24 I. S. Divya, S. Kandasamy, S. Hasebe, T. Sasaki, H. Koshima, K. Wozniak and S. Varughese, Flexible organic crystals. Understanding the tractable co-existence of elastic and plastic bending, *Chem. Sci.*, 2022, **13**, 8989–9003.

25 K. Huang, L. Song, K. Liu, A. Lv, M. Singh, K. Shen, J. Shen, J. Wang, H. Wang, H. Shi, H. Ma, M. Gu, G. Sun, W. Yao, Z. An and W. Huang, Elastic organic crystals with ultralong phosphorescence for flexible anti-counterfeiting, *npj Flexible Electron.*, 2021, **5**, 21–26.

26 K. J. Kalita, S. Mondal, C. M. Reddy and R. K. Vijayaraghavan, Temperature-regulated dual phosphorescence and mechanical strain-induced luminescence modulation in a plastically bendable and twistable organic crystal, *Chem. Mater.*, 2023, **35**, 709–718.

27 D. Tu, J. Zhang, Y. Zhang, H. H. Y. Sung, L. Liu, R. T. K. Kwok, J. W. Y. Lam, I. D. Williams, H. Yan and B. Z. Tang, How do molecular motions affect structures and properties at molecule and aggregate levels?, *J. Am. Chem. Soc.*, 2021, **143**, 11820–11827.

28 S. Bhandary, R. Van Deun, A. M. Kaczmarek and K. Van Hecke, Deformation-induced phosphorescence shift in a 2D elastically flexible organic single crystal: role of chalcogen-centered weak interactions, *Chem. Sci.*, 2022, **13**, 10308–10314.

29 A. Huang, Y. Fan, K. Wang, Z. Wang, X. Wang, K. Chang, Y. Gao, M. Chen, Q. Li and Z. Li, Organic persistent RTP crystals: from brittle to flexible by tunable self-partitioned molecular packing, *Adv. Mater.*, 2023, **35**, e2209166-9.

30 S. Saha and G. R. Desiraju, Acid···amide supramolecular synthon in cocrystals: from spectroscopic detection to property engineering, *J. Am. Chem. Soc.*, 2018, **140**, 6361–6373.

31 K. Zhang, L. Y. Peng, X. X. Liu, X. Xu, W. H. Fang, G. Cui, Y. Z. Chen, C. H. Tung and L. Z. Wu, Aromatic amides: A smart backbone toward isolated ultralong bright blue-phosphorescence in confined polymeric films, *Angew. Chem., Int. Ed.*, 2023, **62**, e202300927-6.

32 G. Xiao, Y. J. Ma, X. Fang and D. Yan, Quadruple anticounterfeiting encryption: anion-modulated forward and reverse excitation-dependent multicolor afterglow in two-component ionic crystals, *ACS Appl. Mater. Interfaces*, 2022, **14**, 30246–30255.

33 J. X. Wang, Y. G. Fang, C. X. Li, L. Y. Niu, W. H. Fang, G. Cui and Q. Z. Yang, Time-dependent afterglow color in a single-component organic molecular crystal, *Angew. Chem., Int. Ed.*, 2020, **59**, 10032–10036.

34 Y. Zhou, L. Jin, J. Chen, W. Hong, G. Liang and W. Qin, Five-in-one: Dual-mode ultralong persistent luminescence with multiple responses from amorphous polymer films, *Chem. Eng. J.*, 2023, **463**, 142506.

35 Z. Yang, Z. Mao, X. Zhang, D. Ou, Y. Mu, Y. Zhang, C. Zhao, S. Liu, Z. Chi, J. Xu, Y.-C. Wu, P.-Y. Lu, A. Lien and M. R. Bryce, Intermolecular electronic coupling of organic units for efficient persistent room-temperature phosphorescence, *Angew. Chem., Int. Ed.*, 2016, **55**, 2181–2185.